nature materials

Article

https://doi.org/10.1038/s41563-026-02495-9

Atomically precise synthesis and simultaneous heterostructure integration of 2D transition metal dichalcogenides through nano-confinement

Received: 23 July 2024

Accepted: 14 January 2026

Ce Bian[1,2,8], **Yifan Zhao**[3,4,8], **Roger Guzman**[2,8], **Hongtao Liu**[1,8], **Hao Hu**[5], **Qi Qi**[1,2], **Ke Zhu**[1,2], **Hao Wang**[1,2], **Kang Wu**[1,2], **Hui Guo**[1], **Wanzhen He**[6], **Zhaoqing Wang**[2], **Peng Peng**[3,7], **Zhiping Xu**[6], **Wu Zhou**[2] ✉, **Feng Ding**[3,4,7] ✉, **Haitao Yang**[1,2] ✉ & **Hong-Jun Gao**[1,2] ✉

Two-dimensional (2D) materials, such as graphene, transition metal dichalcogenides (TMDs) and hexagonal boron nitride, exhibit intriguing properties that are sensitive to their atomic-scale structures and can be further enriched through van der Waals (vdW) integration. However, the precise synthesis and clean integration of 2D materials remain challenging. Here, using graphene or hexagonal boron nitride as a vdW capping layer, we create a nano-confined environment that directs the growth kinetics of 2D TMDs (such as $NbSe_2$ and MoS_2), enabling precise formation of TMD monolayers with tailored morphologies, from isolated monolayer domains to large-scale continuous films and intrinsically patterned rings. Moreover, Janus S–Mo–Se monolayers are synthesized with atomic precision via vdW-protected bottom-plane chalcogen substitution. Importantly, our approach simultaneously produces ultraclean vdW interfaces. This in situ encapsulation reliably preserves air-sensitive materials, as evidenced by the enhanced superconductivity of nano-confined $NbSe_2$ monolayers. Altogether, our study establishes a versatile platform for the controlled synthesis and integration of 2D TMDs for advanced applications.

Two-dimensional (2D) transition metal dichalcogenides (TMDs) and their homo/heterostructures exhibit a plethora of unique physical and chemical properties that enable emerging applications in next-generation electronics[1–5], twistronics[6–9], energy harvesting[10], sensing[11] and catalysis[12]. However, the intriguing properties of 2D TMDs are dictated by their atomic-scale structures, particularly the layer number and the atomic compositions and arrangements. For example, MoS_2 is a direct bandgap semiconductor only in the monolayer form, whereas multilayer MoS_2 undergoes a direct-to-indirect bandgap transition owing to interlayer van der Waals (vdW) coupling[13]. Moreover, monolayer $NbSe_2$, a 2D superconductor, exhibits an extremely high in-plane critical field (~32 T) originating from robust Ising pairing protected by the spin–orbit interaction[14]. With increasing number of $NbSe_2$ layers, the vdW coupling disturbs the perfect Ising pairing and introduces an orbital effect, both of which diminish the critical field[14]. At an even finer level of structural control, sandwiching the transition metal atoms between different chalcogen species (for example, S–Mo–Se) breaks the out-of-plane symmetry and creates a polar Janus TMD monolayer[15–20]. This symmetry breaking leads to a range of intriguing properties (such as piezoelectricity[21], thermoelectricity[22]

A full list of affiliations appears at the end of the paper. ✉e-mail: wuzhou@ucas.ac.cn; dingf@szlab.ac.cn; htyang@iphy.ac.cn; hjgao@iphy.ac.cn

and pyroelectricity[23]), positioning Janus TMD monolayers as a versatile platform for 2D multifunctional devices.

The sensitivity of the intriguing properties of 2D TMDs to their atomic-scale structures necessitates atomically precise synthesis. For monolayer TMDs, precise control over the layer thickness requires effective suppression of adlayer nucleation, which remains challenging owing to a delicate balance between precursor deposition and surface diffusion[24,25] (Supplementary Note 1). The synthesis of Janus TMD monolayers, typically through one-side substitution of their classical counterparts, has not yet achieved atomic precision, as the opposite chalcogen plane can be unintentionally modified due to poorly controlled substitution kinetics[16] (Supplementary Note 2). Furthermore, the application of 2D TMDs often relies on their clean vdW integration with other layered materials (such as graphene and hexagonal boron nitride (hBN)) to preserve inherent properties[14] or enable emergent phenomena[7]. However, conventional transfer methods for fabricating vdW heterostructures can easily introduce interfacial contamination[26], substantially degrading both the inherent and the emergent properties.

In this study, we introduce a nano-confined chemical vapour deposition (CVD) approach that utilizes graphene or hBN as a vdW capping layer, enabling atomically precise synthesis of 2D TMDs along with their simultaneous vdW integration. In contrast to conventional open growth, the nano-confined growth precisely yields $NbSe_2$ and MoS_2 monolayers owing to distinct kinetic mechanisms. The growth morphologies can be tailored from isolated monolayer domains to large-scale continuous films and intrinsically patterned rings by simply tuning the growth conditions. Beyond classical TMDs, Janus MoSSe monolayers can be synthesized by selectively substituting the bottom chalcogen plane, with the top plane protected by the vdW capping layer, demonstrating true atomic-plane selectivity. Importantly, the nano-confined growth simultaneously achieves vdW integration, creating graphene/TMD and hBN/TMD heterostructures with ultraclean vdW interfaces and enabling in situ encapsulation that effectively preserves air-sensitive materials. Benefiting from this reliable encapsulation, our nano-confined $NbSe_2$ monolayers exhibit exceptional air stability and a markedly higher superconducting transition temperature compared with conventional CVD-grown samples. Taken together, our results demonstrate that the nano-confined growth with vdW capping layers provides a versatile platform for the atomically precise synthesis, ultraclean integration and advanced applications of 2D TMDs.

Nano-confined growth of TMD monolayers

The nano-confined growth is schematically illustrated in Fig. 1a. First, graphene or hBN capping layers were mechanically exfoliated onto a SiO_2/Si substrate, creating an interface that served as the nano-confinement for TMD growth (Fig. 1a, left). Next, TMD precursors were produced by ambient-pressure CVD and intercalated into this interface (Fig. 1a, middle). As the precursor concentration increased, nucleation finally occurred, and monolayer TMDs formed with high precision under the confined environment (Fig. 1a, right).

As an example, the nano-confined growth of $NbSe_2$ monolayers is demonstrated underneath graphene capping layers. An optical micrograph of as-grown samples is shown in Fig. 1b, revealing triangular $NbSe_2$ domains with uniform optical contrast. The nano-confined growth scheme is confirmed by cross-sectional scanning transmission electron microscopy (STEM). In the bright-field (BF) STEM image (Fig. 1c,d), two dark stripes, indicated by arrows, are observed above the SiO_2 substrate. The simultaneously acquired high-angle annular dark-field (HAADF) image (Fig. 1e) clearly identifies the lower dark stripe as a $NbSe_2$ monolayer, with its atomic arrangement resolved along the <210> zone axis, and the upper dark stripe as the graphene capping layer, showing weak HAADF intensity consistent with a lower atomic number. This structural assignment is further verified by electron energy-loss spectroscopy (EELS) elemental mappings (Supplementary Fig. 6), collectively evidencing the formation of $NbSe_2$ monolayers underneath graphene.

The nano-confined $NbSe_2$ monolayers were characterized using Raman spectroscopy. Conventional open-grown $NbSe_2$ crystals with a broad thickness distribution[27–29] (Supplementary Fig. 2) were included for comparison. As shown in Fig. 1f, the nano-confined $NbSe_2$ monolayers exhibit the typical A_{1g} and E_{2g} bands at 226 and 250 cm^{-1}, respectively, along with the soft mode around 180 cm^{-1} (ref. 30) (Fig. 1f, red curve and Supplementary Fig. 4). The large A_{1g}–E_{2g} band separation of 24 cm^{-1} is characteristic of $NbSe_2$ monolayers, in contrast to open-grown thick $NbSe_2$ crystals, which show a small separation of 12 cm^{-1} (ref. 30) (Fig. 1f, blue curve). Importantly, atomically thin $NbSe_2$ crystals are highly air-sensitive[31,32], as evidenced by the barely detectable Raman bands of open-grown $NbSe_2$ monolayers (Fig. 1f, grey curve). In contrast, the nano-confined $NbSe_2$ monolayers are in situ encapsulated and maintain sharp Raman bands even after 60 days of air exposure (Fig. 1f, purple curve and Supplementary Figs. 10 and 11). This exceptional air stability enables both extensive characterization and reliable device integration of the nano-confined $NbSe_2$ monolayers, markedly broadening their application potential.

The monolayer yields of different growth schemes are compared in Fig. 1g. Remarkably, 98% of nano-confined $NbSe_2$ crystals are monolayers, whereas open-grown counterparts exhibit a monolayer yield of only 41%. This contrast highlights distinct growth mechanisms under the nano-confinement, enabling precise monolayer formation regardless of macroscopic growth conditions.

Mechanisms of the nano-confined growth

The nano-confined growth mechanisms were analysed from both energetic and kinetic perspectives. Energetically, the binding energy of $NbSe_2$ monolayers was calculated using density functional theory (DFT) for different growth schemes, including the nano-confined growth (graphene/$NbSe_2$/SiO_2), the open growth on SiO_2 ($NbSe_2$/SiO_2) and the open growth on graphene ($NbSe_2$/graphene/SiO_2), with various SiO_2 terminations to model the amorphous substrate[33] (Supplementary Tables 2 and 3). As shown in Fig. 2a, the nano-confined $NbSe_2$ monolayers exhibit the most negative binding energy regardless of SiO_2 terminations (such as −0.97 eV per Nb for nano-confined growth versus −0.80 eV per Nb for open growth on Si-terminated SiO_2), demonstrating energetically favoured growth under the nano-confinement, consistent with interactions at both interfaces of the TMD monolayers[34] (Supplementary Fig. 13).

From the kinetic perspective, the nano-confined growth relies on effective intercalation of precursors, which dictates the morphology of TMD crystals. Our study reveals two distinct morphologies: (1) triangular domains evenly distributed across graphene capping layers (Fig. 1b and Supplementary Fig. 18a) and (2) domains preferentially nucleated near graphene edges (Supplementary Fig. 2a). The former is attributed to surface intercalation of precursors facilitated by point defects or tears in the graphene basal plane, whereas the latter corresponds to intact graphene capping layers with the edges serving as the only intercalation paths. In this case, precursors diffuse directionally from the edges toward the interior, leading to asymmetric growth shapes of the nano-confined TMD crystals.

To confirm this edge-intercalation mechanism on the basis of the symmetry of growth shapes, side lengths of triangular $NbSe_2$ monolayers were extracted from optical micrographs, and the degree of growth asymmetry (DGA) was quantified as follows:

$$\mathrm{DGA} = \frac{\max_{i \neq j} |l_i - l_j|}{L}, \quad (1)$$

where l_i ($i = 1, 2$ and 3) are the side lengths and L is their average value. The crystal-to-edge distance (d) and the overgrowth direction (φ) were extracted according to definitions shown in the inset of Fig. 2b. The relationship between DGA and d is shown in the main panel of Fig. 2b,

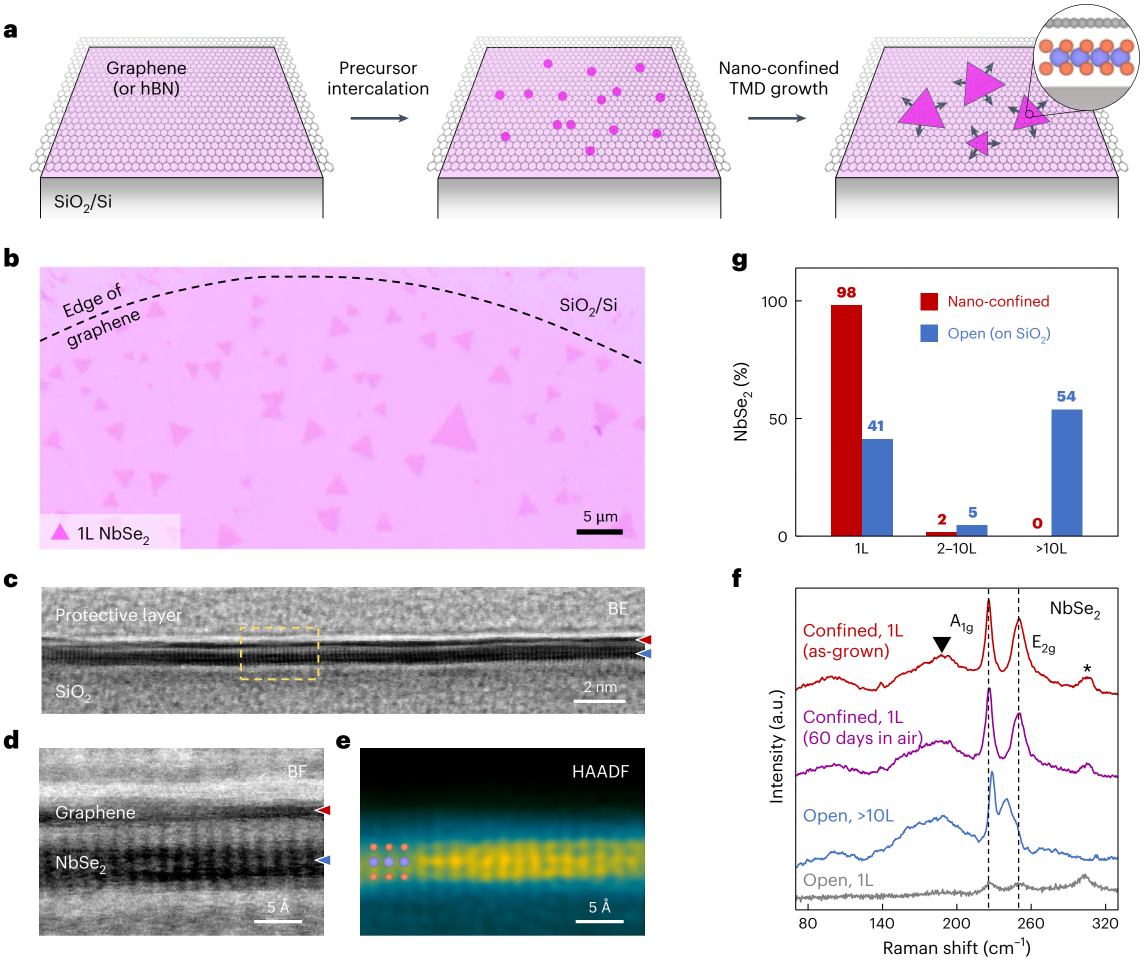

Fig. 1 | Nano-confined growth of NbSe$_2$ monolayers. a, A schematic diagram illustrating the growth procedure. **b**, An optical micrograph of NbSe$_2$ monolayers grown underneath a graphene monolayer. **c**–**e**, Cross-sectional STEM characterizations: large-scale BF image (**c**) and close-up BF (**d**) and HAADF (**e**) images of the dashed region in **c**. The arrows in the BF images **c** and **d** indicate dark stripes from graphene (red arrowhead) and NbSe$_2$ (blue arrowhead) monolayers. The atomic model of a NbSe$_2$ monolayer along the <210> zone axis is overlaid on the HAADF image (**e**), with the purple and orange balls representing the Nb and Se atoms, respectively. **f**, Raman spectra of nano-confined NbSe$_2$ monolayers and open-grown NbSe$_2$ crystals with different thicknesses. The dashed lines indicate the typical bands of NbSe$_2$ monolayers. ▼ and * indicate the NbSe$_2$ soft mode and the Si band, respectively. All spectra were collected under ambient conditions and right after growth unless otherwise specified. **g**, Thickness distributions of NbSe$_2$ crystals grown under the nano-confinement and on open SiO$_2$ substrates. *n*L denotes *n* layer(s).

with φ indicated by the colour scale. Remarkably, highly asymmetric NbSe$_2$ crystals with DGA >0.2 predominantly overgrow toward graphene edges ($0° < \varphi < 90°$) (Fig. 2b, red), highlighting the edges as effective intercalation paths and the directional precursor diffusion that promotes overgrowth at edge-facing vertices[35,36]. Consistently, our phase-field simulations incorporating edge intercalation reproduce this asymmetric growth behaviour (Supplementary Fig. 14), further confirming the edge-intercalation mechanism.

Following edge intercalation and directional diffusion, the confined environment enables precursor incorporation exclusively through in-plane edge attachment (Fig. 2c), naturally preventing adlayer nucleation and ensuring precise monolayer formation. This contrasts with open CVD growth, where vaporized precursors are deposited directly onto the surface of TMD monolayers and readily form adlayers unless the deposition rate is stringently controlled[36] (Fig. 2d and Supplementary Note 1). These results underscore the distinct growth kinetics under the nano-confinement, enabling precise synthesis of monolayer TMDs.

Atomically precise synthesis

Following the procedure shown in Fig. 1a, the nano-confined growth can be readily extended to other classical TMD monolayers (such as MoS$_2$; Supplementary Figs. 2, 4, 7 and 12), as well as to the use of CVD-grown graphene (Supplementary Fig. 3) and insulating hBN (Supplementary Figs. 2, 4, 8, 9 and 11) as the vdW capping layers, all governed by consistent energetic (Fig. 2a and Supplementary Tables 2–5) and kinetic (Fig. 2c and Supplementary Figs. 2, 3 and 14) mechanisms. Moreover, the material library can be expanded to include Janus TMD monolayers featuring the polar chalcogen arrangement, for which the precision of the nano-confined growth reaches the atomic limit.

To date, the synthesis of Janus TMD monolayers has relied on the one-side substitution of classical TMD monolayers[15–20]. The challenge is that the Janus phase is not energetically favoured compared with the alloy phase resulting from random, two-side substitution (Fig. 3a). The energy difference between the one-side and two-side substitution products, defined as $\Delta E = E_{\text{one-side}} - E_{\text{two-side}}$, was calculated using DFT for different substitution ratios (Supplementary Tables 6 and 7). The upper (lower) panel of Fig. 3b presents ΔE for $MoS_{2(1-x)}Se_{2x}$ ($MoS_{2x}Se_{2(1-x)}$) monolayers, where $0 \le x \le 0.5$ is the substitution ratio, with the lower and upper bounds denoting the pristine and half-substituted MoS$_2$ (MoSe$_2$) monolayer, respectively. Evidently, ΔE is always positive (that is, $E_{\text{one-side}} > E_{\text{two-side}}$) and continuously increases with x, indicating that the one-side substitution of a classical TMD monolayer toward a Janus TMD monolayer is energetically unfavoured, hence the key to realise

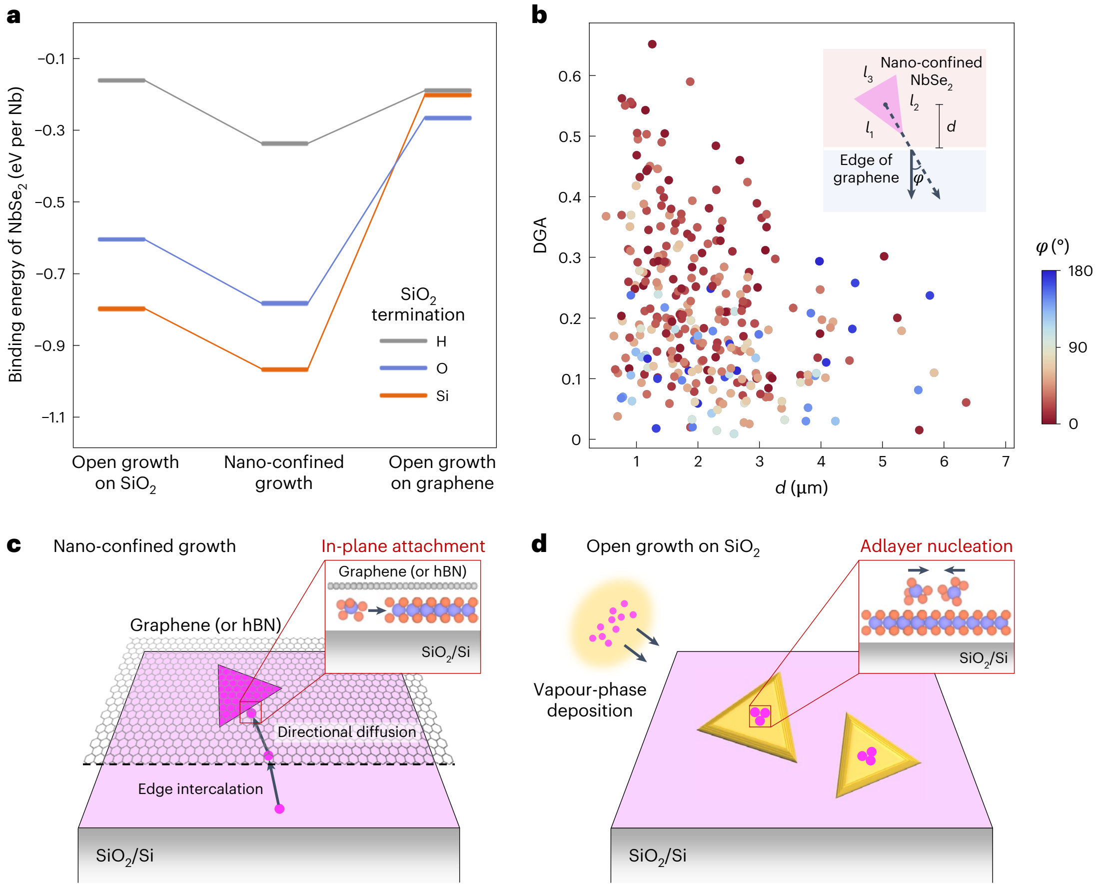

Fig. 2 | Mechanisms of the nano-confined growth. a, A comparison of the binding energy of $NbSe_2$ monolayers across different growth schemes, considering various SiO_2 terminations. **b**, The relationship between the DGA and the crystal-to-edge distance (d), with the colour scale indicating the overgrowth direction (φ). Inset: definitions of d and φ, as well as the side lengths (l_1, l_2 and l_3) for determining DGA according to equation (1). The overgrowth direction (dashed arrow), pointing from the centre of the crystal (dot) to the overgrown vertex (intersection of l_1 and l_2), is measured relative to the graphene edge normal (solid arrow). **c**,**d**, Schematic diagrams illustrating growth kinetics for uniform TMD monolayers under the nano-confinement (**c**) and for multilayer TMD crystals on open SiO_2 substrates (**d**). The dashed line in **c** indicates the edge of the capping layer.

the Janus phase is to control the substitution by kinetics rather than by energetics[15].

We demonstrate that nano-confinement can be utilized to control the substitution kinetics, enabling the atomically precise synthesis of Janus MoSSe monolayers. The process involves MoS_2 monolayers grown underneath graphene or hBN, with $NbSe_2$ precursors serving as substitution agents to supply Se atoms. Direct attachment of $NbSe_2$ precursors to the edges of MoS_2 monolayers is unlikely because of their substantial lattice mismatch (~9%)[37]. Instead, $NbSe_2$ precursors selectively intercalate into the MoS_2–SiO_2 interface, rather than into the vdW gap between graphene or hBN and MoS_2, owing to their distinct interfacial properties (Supplementary Note 3). As a result, only the bottom S plane is exposed to Se atoms, making the one-side substitution of the bottom S plane kinetically favoured[17].

The as-synthesized Janus MoSSe monolayers were first characterized using Raman spectroscopy. As shown in Fig. 3c (lower panel) the sharp A_1^1 Raman band at 290 cm^{-1} arises from the out-of-plane vibrations of the S–Mo–Se bond[38], and the absence of MoS_2-related Raman bands (383 and 406 cm^{-1}) (Fig. 3c, upper panel) demonstrates complete one-side substitution. Photoluminescence (PL) spectra before and after the substitution are compared in Fig. 3d. The emission peak shifts from 1.83 eV (MoS_2) to 1.72 eV (Janus MoSSe), agreeing with previous reports[19]. The notably narrower Raman and PL linewidths compared with literature values demonstrate the superior crystal quality of the as-synthesized Janus MoSSe monolayers (Supplementary Fig. 23). In addition, the superior substitution uniformity is confirmed by uniform Raman and PL intensities across the Janus MoSSe monolayers (Fig. 3c,d, right insets). As the one-side substitution preserves the in-plane crystal symmetry, similar sixfold variations are observed in the polarization-resolved second-harmonic generation (SHG) intensity for both the Janus MoSSe monolayers (Fig. 3e,f and Supplementary Fig. 16) and the MoS_2 monolayers[39] (Supplementary Fig. 12). In contrast, the out-of-plane crystal symmetry is broken by the one-side substitution, as directly revealed by cross-sectional HAADF-STEM. An atomically resolved HAADF image of the graphene-confined Janus MoSSe monolayer is shown in Fig. 3g (see Supplementary Fig. 15 for the HAADF image of the hBN-confined sample). A close observation demonstrates that the chalcogen atoms on the two sides of the monolayer exhibit different HAADF intensities (Supplementary Fig. 15): the atoms on the lower side, showing stronger intensities, are identified as Se, whereas the upper atoms with weaker intensities are assigned to S. The corresponding HAADF simulation, overlaid on the dashed region in Fig. 3g, agrees with the experimental image. These results demonstrate the one-side substitution of the bottom S atoms, confirming the selective intercalation of $NbSe_2$ precursors into the MoS_2–SiO_2 interface (Fig. 3g, inset). Benefiting from the vdW capping layer, the top chalcogen atoms are effectively protected from unintentional modification, enabling the atomically precise synthesis of high-quality Janus TMD monolayers, as evidenced by their narrow optical emission.

Moreover, the vdW gap between graphene and the Janus MoSSe monolayer was determined to be 3.7 Å (Fig. 3g), closely matching our DFT-calculated value of 3.4 Å (Supplementary Fig. 15), indicating an

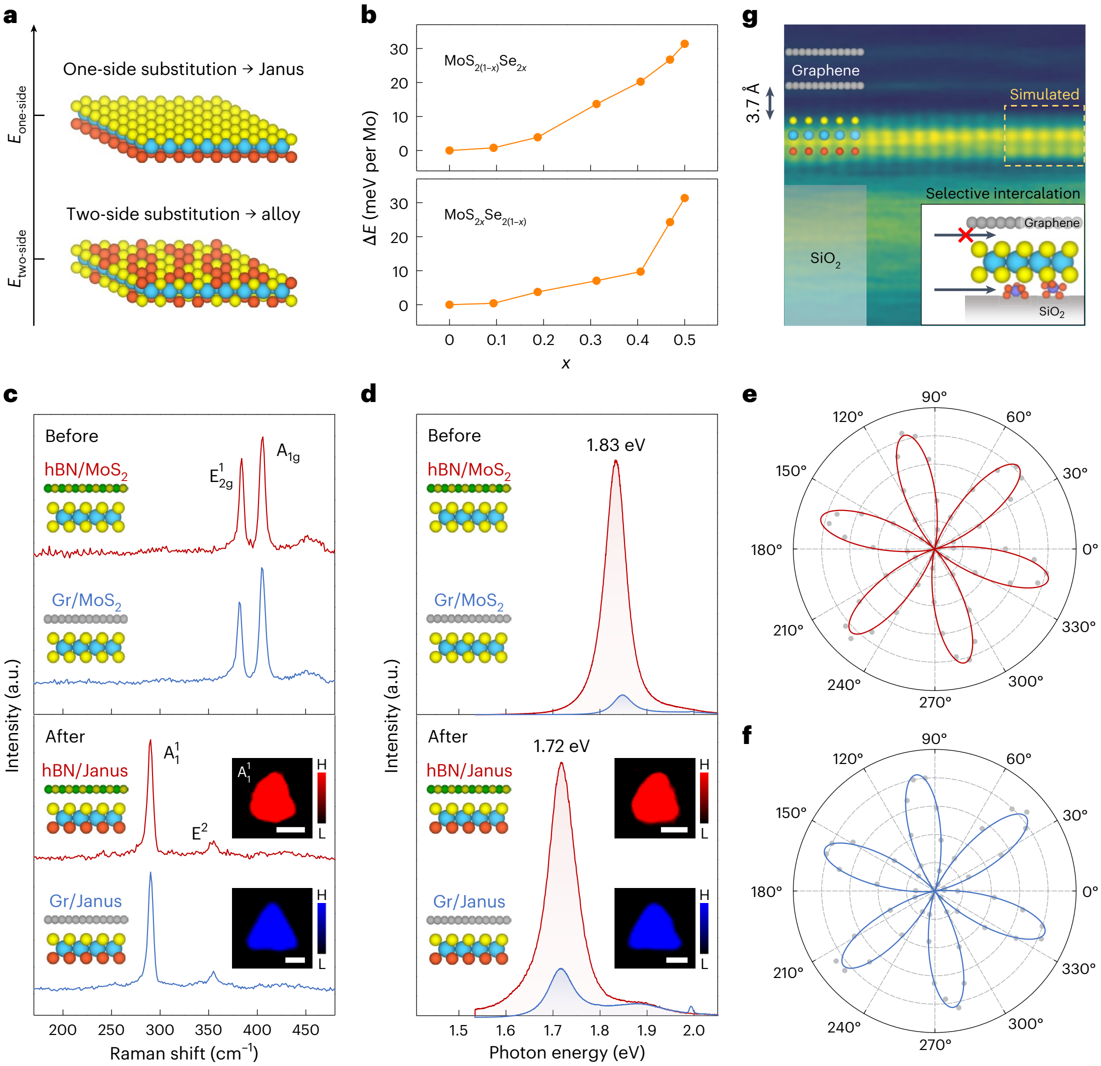

Fig. 3 | Atomically precise synthesis of Janus MoSSe monolayers under nano-confinement. a, A comparison of the Janus and alloy phases resulting from one-side and two-side substitutions of a classical TMD monolayer. **b**, The substitution energy difference, defined as $\Delta E = E_{\text{one-side}} - E_{\text{two-side}}$, calculated for $MoS_{2(1-x)}Se_{2x}$ and $MoS_{2x}Se_{2(1-x)}$ (upper and lower panels, respectively). **c**,**d**, Raman (**c**) and PL (**d**) spectra of the as-synthesized MoS_2 monolayers (upper panels) and the Janus MoSSe monolayers after the substitution (lower panels), with either hBN or graphene (Gr) as the capping layer. Left insets: sample schematics. Right insets: Raman and PL mappings. H and L denote high and low intensity, respectively. All scale bars are 1 µm. **e**,**f**, Polarization-resolved SHG intensities of the Janus MoSSe monolayers synthesized with hBN (**e**) or graphene (**f**) capping layers. The smooth curves represent fits to the data (Supplementary Fig. 16). **g**, A cross-sectional HAADF-STEM image of the graphene-confined Janus MoSSe monolayer, with a sample schematic overlaid on the left and a simulated HAADF image shown on the right. Bottom right inset: schematic diagram illustrating the selective intercalation of precursors. The C, Mo, S, Nb and Se atoms are represented by the grey, cyan, yellow, purple and orange balls, respectively.

ultraclean vdW interface enabled by the simultaneous integration. This clean contact allows interfacial charge transfer, resulting in PL quenching in the graphene-confined Janus MoSSe monolayers, with similar behaviour observed in the MoS_2/graphene heterostructures[40] (Fig. 3d). This contrasts with the hBN-confined monolayers, which exhibit strongly enhanced PL emission owing to the insulating nature of hBN. In addition, photoinduced doping governs the photoresponse of the graphene/Janus MoSSe heterostructure device, which provides further evidence of charge transfer and highlights its potential for emerging 2D optoelectronic applications (Supplementary Fig. 22).

Intrinsically patterned growth

By increasing the deposition flux of precursors to promote coalescence of isolated TMD domains, the nano-confined growth can be extended to two distinct growth regimes: (1) large-scale synthesis of continuous TMD films under defective capping layers that facilitate homogeneous nucleation (Supplementary Fig. 18) and (2) intrinsically patterned growth of TMD rings under intact capping layers that direct nucleation near their edges (Supplementary Fig. 19). These growth morphologies are captured in a kinetic phase diagram defined by the defect density in the capping layers and the precursor deposition flux (Supplementary Fig. 17). Notably, the intrinsic patterning regime enables the precise synthesis of patterned TMD monolayers simply by designing the capping layer geometry, avoiding post-synthesis lithography or etching processes that often degrade the monolayer quality.

Figure 4a–c shows optical micrographs of intrinsically patterned $NbSe_2$ monolayers, which clearly follow the edge contours of the hBN capping layers with regular geometric shapes. Corresponding Raman mappings shown in Fig. 4d–f demonstrate uniform intensity across the $NbSe_2$ rings, which confirms their structural continuity and enables their application as conductive channels in 2D circuits. As a proof-of-concept, devices were fabricated from the intrinsically

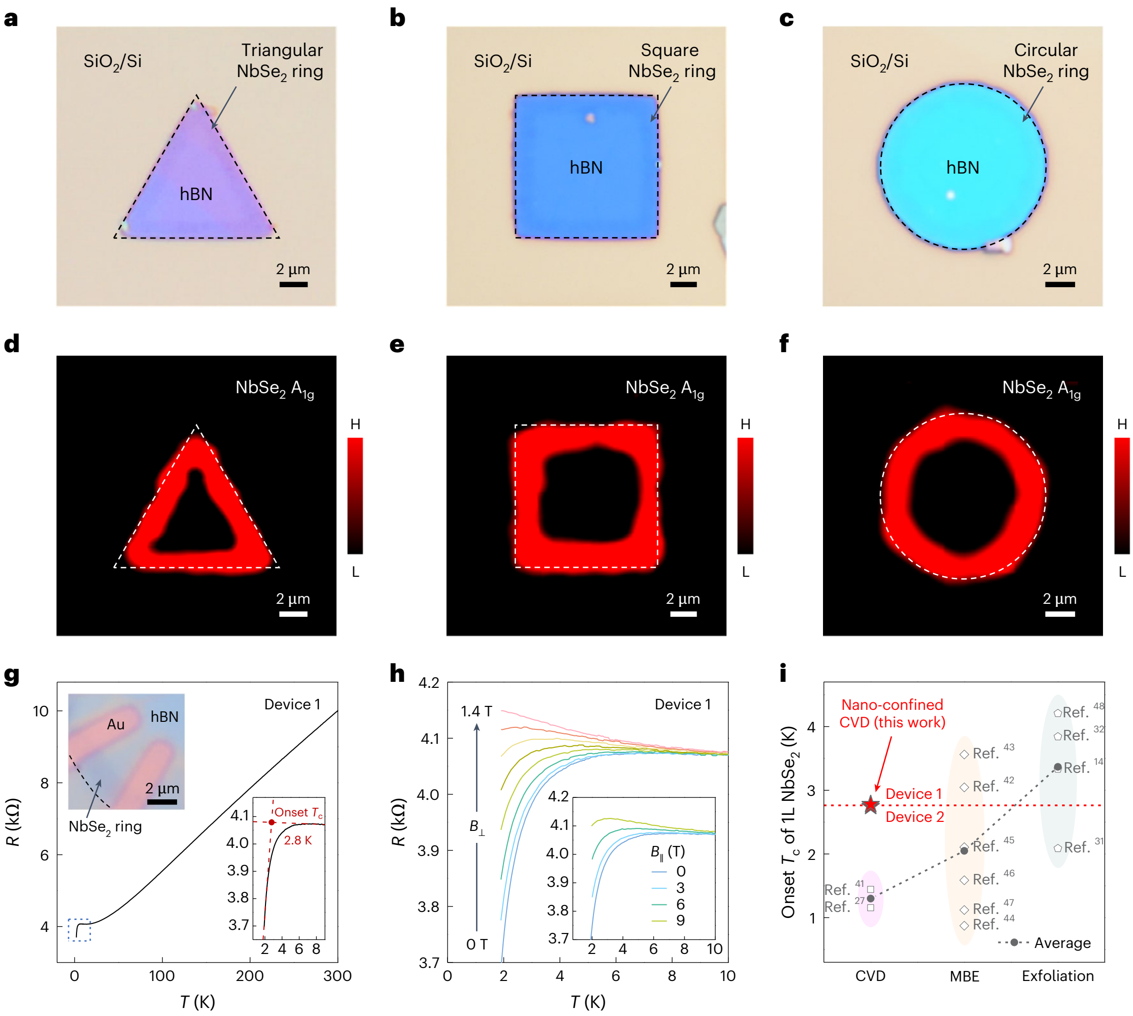

Fig. 4 | Intrinsically patterned growth of NbSe$_2$ monolayers. a–f, Optical micrographs (**a**–**c**) and Raman mappings (**d**–**f**) showing intrinsically patterned NbSe$_2$ monolayer rings grown underneath hBN flakes with regular triangle (**a** and **d**), square (**b** and **e**) and circle (**c** and **f**) shapes. Dashed lines in **a**–**f** indicate hBN edges. **g**, The resistance–temperature (R–T) curve of the intrinsically patterned NbSe$_2$ ring. Bottom right inset: close-up of the low-T region (marked by dashed lines in the main panel), which highlights the onset of the superconducting transition. Top-left inset: optical micrograph of the device. The hBN edge is indicated by the dashed line. **h**, R–T curves measured under perpendicular and parallel magnetic fields (main panel and inset, respectively). **i**, The comparison of onset T_c values for NbSe$_2$ monolayers fabricated using different methods. Average values from this work and literature are represented by red and grey dashed lines, respectively. Device 2 data are provided in Supplementary Fig. 20.

patterned NbSe$_2$ rings by transferring the hBN/NbSe$_2$ heterostructures onto bottom metal electrodes. An optical micrograph of a typical device is shown in Fig. 4g (top left inset). The main panel presents the temperature-dependent resistance, which reveals a linear relationship consistent with the metallic nature of NbSe$_2$, followed by a sharp superconducting transition with an onset transition temperature (T_c) of 2.8 K (Fig. 4g, bottom right inset). Under perpendicular magnetic fields, the superconducting transition is quickly suppressed (Fig. 4h), whereas it is substantially more robust under parallel fields (Fig. 4h, inset) owing to robust Ising pairing protected by the spin–orbit interaction[14]. To assess the superconducting performance of our NbSe$_2$ monolayers, the onset T_c was benchmarked against that of samples fabricated using alternative methods. As shown in Fig. 4i, the onset T_c of our NbSe$_2$ monolayers markedly exceeds those synthesized using conventional CVD[27,41], matches molecular-beam epitaxy (MBE)-grown samples[42–47] and even approaches mechanically exfoliated NbSe$_2$ monolayers[14,31,32,48]. Such excellent performance highlights the enhanced uniformity, superior quality and exceptional stability of our NbSe$_2$ monolayers (Supplementary Table 9), paving the way for their applications in superconducting circuits.

Conclusions

We establish a nano-confined approach to synthesising TMD monolayers using graphene or hBN as the vdW capping layer. The growth mechanisms are governed by distinct kinetics—including edge intercalation, directional diffusion and in-plane attachment of precursors—which naturally ensure the precise formation of monolayers, achieving a high yield of 98% for NbSe$_2$. The realization of Janus MoSSe monolayers through vdW-protected substitution on a single chalcogen plane of MoS$_2$ highlights the atomic-level precision of the nano-confined synthesis. The vdW capping layers also serve as in situ encapsulation, effectively preserving the superior crystal quality of the air-sensitive NbSe$_2$ monolayers. This enables exceptional air stability for over 60 days and allows the observation of enhanced superconducting performance, with an onset T_c of 2.8 K that markedly exceeds reported values for CVD-grown NbSe$_2$ monolayers. Altogether, the nano-confined growth offers a platform for the atomically precise synthesis and simultaneous integration of monolayer TMDs (Supplementary Table 8). We note that wafer-scale CVD growth of graphene and hBN has been well established[49,50], and the resulting films can be transferred onto SiO$_2$/Si substrates with high cleanliness and uniformity[51,52]. Integrating these mature technologies for the capping layers with the nano-confined growth should enable wafer-scale synthesis of continuous TMD films when basal-plane defects are controllably introduced into the capping layers[53,54], as well as the scalable fabrication of TMD-based 2D circuits by leveraging the unique intrinsic patterning capability.

Online content

Any methods, additional references, Nature Portfolio reporting summaries, source data, extended data, supplementary information, acknowledgements, peer review information; details of author contributions and competing interests; and statements of data and code availability are available at https://doi.org/10.1038/s41563-026-02495-9.

References

1. Zou, X. et al. Robust epitaxy of single-crystal transition-metal dichalcogenides on lanthanum-passivated sapphire. *Science* **390**, eaea0849 (2025).
2. Moon, D. et al. Hypotaxy of wafer-scale single-crystal transition metal dichalcogenides. *Nature* **638**, 957–964 (2025).
3. Zhou, Z. et al. Stack growth of wafer-scale van der Waals superconductor heterostructures. *Nature* **621**, 499–505 (2023).
4. Liu, L. et al. Uniform nucleation and epitaxy of bilayer molybdenum disulfide on sapphire. *Nature* **605**, 69–75 (2022).
5. Li, J. et al. General synthesis of two-dimensional van der Waals heterostructure arrays. *Nature* **579**, 368–374 (2020).
6. Park, H. et al. Observation of fractionally quantized anomalous Hall effect. *Nature* **622**, 74–79 (2023).
7. Lin, J.-X. et al. Spin–orbit-driven ferromagnetism at half moiré filling in magic-angle twisted bilayer graphene. *Science* **375**, 437–441 (2022).
8. Weston, A. et al. Interfacial ferroelectricity in marginally twisted 2D semiconductors. *Nat. Nanotechnol.* **17**, 390–395 (2022).
9. Wang, L. et al. Correlated electronic phases in twisted bilayer transition metal dichalcogenides. *Nat. Mater.* **19**, 861–866 (2020).
10. Zai, H. et al. Wafer-scale monolayer MoS_2 film integration for stable, efficient perovskite solar cells. *Science* **387**, 186–192 (2025).
11. Mennel, L. et al. Ultrafast machine vision with 2D material neural network image sensors. *Nature* **579**, 62–66 (2020).
12. He, Y. et al. Amorphizing noble metal chalcogenide catalysts at the single-layer limit towards hydrogen production. *Nat. Catal.* **5**, 212–221 (2022).
13. Cappelluti, E., Roldán, R., Silva-Guillén, J. A., Ordejón, P. & Guinea, F. Tight-binding model and direct-gap/indirect-gap transition in single-layer and multilayer MoS_2. *Phys. Rev. B* **88**, 075409 (2013).
14. Xi, X. et al. Ising pairing in superconducting $NbSe_2$ atomic layers. *Nat. Phys.* **12**, 139–143 (2015).
15. Lu, A.-Y. et al. Janus monolayers of transition metal dichalcogenides. *Nat. Nanotechnol.* **12**, 744–749 (2017).
16. Zhang, J. et al. Janus monolayer transition-metal dichalcogenides. *ACS Nano* **11**, 8192–8198 (2017).
17. Lin, Y.-C. et al. Low energy implantation into transition-metal dichalcogenide monolayers to form Janus structures. *ACS Nano* **14**, 3896–3906 (2020).
18. Trivedi, D. B. et al. Room-temperature synthesis of 2D Janus crystals and their heterostructures. *Adv. Mater.* **32**, 2006320 (2020).
19. Guo, Y. et al. Designing artificial two-dimensional landscapes via atomic substitution. *Proc. Natl Acad. Sci. USA* **118**, e2106124118 (2021).
20. Gan, Z. et al. Chemical vapor deposition of high-optical-quality large-area monolayer Janus transition metal dichalcogenides. *Adv. Mater.* **34**, 2205226 (2022).
21. Dong, L., Lou, J. & Shenoy, V. B. Large in-plane and vertical piezoelectricity in Janus transition metal dichalchogenides. *ACS Nano* **11**, 8242–8248 (2017).
22. Patel, A., Singh, D., Sonvane, Y., Thakor, P. B. & Ahuja, R. High thermoelectric performance in two-dimensional Janus monolayer material WS-X (X = Se and Te). *ACS Appl. Mater. Interfaces* **12**, 46212–46219 (2020).
23. Liu, J. & Pantelides, S. T. Mechanisms of pyroelectricity in three- and two-dimensional materials. *Phys. Rev. Lett.* **120**, 207602 (2018).
24. Kang, K. et al. High-mobility three-atom-thick semiconducting films with wafer-scale homogeneity. *Nature* **520**, 656–660 (2015).
25. Seol, M. et al. High-throughput growth of wafer-scale monolayer transition metal dichalcogenide via vertical Ostwald ripening. *Adv. Mater.* **32**, 2003542 (2020).
26. Haigh, S. J. et al. Cross-sectional imaging of individual layers and buried interfaces of graphene-based heterostructures and superlattices. *Nat. Mater.* **11**, 764–767 (2012).
27. Wang, H. et al. High-quality monolayer superconductor $NbSe_2$ grown by chemical vapour deposition. *Nat. Commun.* **8**, 394 (2017).
28. Zou, Y.-C. et al. Superconductivity and magnetotransport of single-crystalline $NbSe_2$ nanoplates grown by chemical vapour deposition. *Nanoscale* **9**, 16591–16595 (2017).
29. Park, S. et al. Tailoring Domain Morphology in Monolayer $NbSe_2$ and $W_xNb_{1-x}Se_2$ Heterostructure. *ACS Nano* **14**, 8784–8792 (2020).
30. Hill, H. M. et al. Comprehensive optical characterization of atomically thin $NbSe_2$. *Phys. Rev. B* **98**, 165109 (2018).
31. Cao, Y. et al. Quality heterostructures from two-dimensional crystals unstable in air by their assembly in inert atmosphere. *Nano Lett.* **15**, 4914–4921 (2015).
32. Telford, E. J. et al. Via method for lithography free contact and preservation of 2D materials. *Nano Lett.* **18**, 1416–1420 (2018).
33. Rudenko, A. N., Keil, F. J., Katsnelson, M. I. & Lichtenstein, A. I. Interfacial interactions between local defects in amorphous SiO_2 and supported graphene. *Phys. Rev. B* **84**, 085438 (2011).
34. Li, J. et al. Wafer-scale single-crystal monolayer graphene grown on sapphire substrate. *Nat. Mater.* **21**, 740–747 (2022).
35. Xiao, R.-F., Alexander, J. I. D. & Rosenberger, F. Growth morphology with anisotropic surface kinetics. *J. Crystal Growth* **100**, 313–329 (1990).
36. Michely, T. & Krug, J. *Islands, Mounds, and Atoms: Patterns and Processes in Crystal Growth Far from Equilibrium* (Springer, 2004).
37. Conte, F., Ninno, D. & Cantele, G. Electronic properties and interlayer coupling of twisted $MoS_2/NbSe_2$ heterobilayers. *Phys. Rev. B* **99**, 155429 (2019).
38. Petrić, M. M. et al. Raman spectrum of Janus transition metal dichalcogenide monolayers WSSe and MoSSe. *Phys. Rev. B* **103**, 035414 (2021).
39. Petrić, M. M. et al. Nonlinear dispersion relation and out-of-plane second harmonic generation in MoSSe and WSSe Janus monolayers. *Adv. Optical Mater.* **11**, 2300958 (2023).
40. Yang, B. et al. Effect of distance on photoluminescence quenching and proximity-induced spin–orbit coupling in graphene/WSe_2 heterostructures. *Nano Lett.* **18**, 3580–3585 (2018).
41. Zhou, J. et al. A library of atomically thin metal chalcogenides. *Nature* **556**, 355–359 (2018).
42. Yi, H. et al. Crossover from Ising- to Rashba-type superconductivity in epitaxial Bi_2Se_3/monolayer $NbSe_2$ heterostructures. *Nat. Mater.* **21**, 1366–1372 (2022).
43. Xing, Y. et al. Ising superconductivity and quantum phase transition in macro-size monolayer $NbSe_2$. *Nano Lett.* **17**, 6802–6807 (2017).
44. Ugeda, M. M. et al. Characterization of collective ground states in single-layer $NbSe_2$. *Nat. Phys.* **12**, 92–97 (2015).
45. Onishi, S. et al. Selenium capped monolayer $NbSe_2$ for two-dimensional superconductivity studies. *Phys. Status Solidi B* **253**, 2396–2399 (2016).

46. Nakata, Y. et al. Anisotropic band splitting in monolayer $NbSe_2$: implications for superconductivity and charge density wave. *npj 2D Mater. Appl.* **2**, 12 (2018).
47. Calavalle, F. et al. Tailoring superconductivity in large-area single-layer $NbSe_2$ via self-assembled molecular adlayers. *Nano Lett.* **21**, 136–143 (2020).
48. Cho, C.-w. et al. Nodal and nematic superconducting phases in $NbSe_2$ monolayers from competing superconducting channels. *Phys. Rev. Lett.* **129**, 087002 (2022).
49. Xu, X. et al. Ultrafast epitaxial growth of metre-sized single-crystal graphene on industrial Cu foil. *Sci. Bull.* **62**, 1074–1080 (2017).
50. Wang, L. et al. Epitaxial growth of a 100-square-centimetre single-crystal hexagonal boron nitride monolayer on copper. *Nature* **570**, 91–95 (2019).
51. Hu, Z. et al. Rapid and scalable transfer of large-area graphene wafers. *Adv. Mater.* **35**, 2300621 (2023).
52. Chen, T.-A. et al. Wafer-scale single-crystal hexagonal boron nitride monolayers on Cu (111). *Nature* **579**, 219–223 (2020).
53. Nan, H. Y. et al. The thermal stability of graphene in air investigated by Raman spectroscopy. *J. Raman Spectrosc.* **44**, 1018–1021 (2013).
54. Na, Y. S. et al. Modulation of optical and electrical properties in hexagonal boron nitride by defects induced via oxygen plasma treatment. *2D Mater.* **8**, 045041 (2021).

---

[1]Beijing National Center for Condensed Matter Physics and Institute of Physics, Chinese Academy of Sciences, Beijing, China. [2]School of Physical Sciences, University of Chinese Academy of Sciences, Beijing, China. [3]Suzhou Laboratory, Suzhou, China. [4]Institute of Technology for Carbon Neutrality, Shenzhen Institute of Advanced Technology, Chinese Academy of Sciences, Shenzhen, China. [5]Frontier Institute of Science and Technology, Xi'an Jiaotong University, Xi'an, China. [6]Department of Engineering Mechanics and Center for Nano and Micro Mechanics, Tsinghua University, Beijing, China. [7]Faculty of Materials Science and Energy Engineering, Shenzhen University of Advanced Technology, Shenzhen, China. [8]These authors contributed equally: Ce Bian, Yifan Zhao, Roger Guzman, Hongtao Liu. ✉e-mail: wuzhou@ucas.ac.cn; dingf@szlab.ac.cn; htyang@iphy.ac.cn; hjgao@iphy.ac.cn

Methods

Preparation of capping layers

Graphene and hBN flakes were mechanically exfoliated onto 285-nm SiO_2/Si substrates using the Scotch tape method. The as-exfoliated samples were annealed under vacuum ($<5 \times 10^{-1}$ Pa) at 500 °C for 1 h to remove tape residue.

Nano-confined growth of $NbSe_2$ monolayers

The nano-confined growth of $NbSe_2$ monolayers was conducted using an ambient-pressure CVD system equipped with a two-zone tube furnace (Supplementary Fig. 1 and Supplementary Table 1). The Nb source, a well-ground powder of Nb_2O_5, Nb and NaCl (weight ratio of 2:2:1; ~2 mg), was placed in a quartz boat, and the graphene- or hBN-covered SiO_2/Si substrate was placed above the powder with the polished surface facing down. This quartz boat was loaded into the downstream zone. Se powder (~0.1 g) in another quartz boat was loaded into the upstream zone. After purging the quartz tube with a mix of 10% H_2/Ar for 10 min, the up- and downstream zones were heated to 220 and 805 °C in 15 min, respectively, and held for 3–5 min before being cooled down to room temperature naturally. A mix of 10% H_2/Ar with a flow rate of 150 standard cubic centimetres per minute (SCCM) was used as the carrier gas. The open-grown $NbSe_2$ crystals were obtained on bare regions of the SiO_2/Si substrate without being covered by graphene or hBN flakes.

Nano-confined growth of MoS_2 monolayers

The nano-confined growth of MoS_2 monolayers was conducted using a similar CVD system (Supplementary Fig. 1 and Supplementary Table 1). A thin film of MoO_3 grown on mica was used as the Mo source. The MoO_3 film was placed in a quartz boat, and the SiO_2/Si substrate was placed above the MoO_3 film. This quartz boat was loaded into the downstream zone, and another quartz boat containing S powder (~0.2 g) was loaded into the upstream zone. The quartz tube was then purged with Ar for 10 min, after which the up- and downstream zones were heated to 140 and 850 °C in 20 min, respectively, and held for 10–15 min before they were naturally cooled down to room temperature. Ar (100 SCCM) was used as the carrier gas.

Nano-confined growth of Janus MoSSe monolayers

To synthesize Janus MoSSe monolayers, an as-grown MoS_2 sample was loaded into the CVD system of $NbSe_2$ and placed in the downstream zone (Supplementary Fig. 1 and Supplementary Table 1). All steps and parameters remained unchanged except for the downstream-zone temperature, which was reduced to 750 °C to suppress $NbSe_2$ growth while still allowing the substitution.

Intrinsically patterned growth

Intrinsically patterned growth requires both intact capping layers and high deposition flux. The integrity of the capping layers was ensured by using multilayer flakes, which effectively prevent point defects and tears from penetrating through the basal plane, and the high deposition flux was achieved by increasing the amount of the transition metal source. For the intrinsically patterned growth of $NbSe_2$ monolayers underneath hBN, multilayer hBN flakes were predefined into regular geometric shapes using photolithography (Karl Suss MA6/BA6) followed by CHF_3/O_2 reactive-ion etching (RIE; Oxford Instruments Plasmalab80Plus). The resulting hBN flakes were placed above the Nb source with the amount increased to ~20 mg to achieve the high flux condition (Supplementary Table 1). All other steps and parameters followed those described for $NbSe_2$ growth.

Sample characterizations

Optical micrographs were obtained using a 100× objective lens of an Olympus BX51 microscope equipped with a halogen light source and an SC30 colour camera. The optical contrast of crystals extracted from the optical micrographs was used to determine the crystal thickness (Supplementary Fig. 5). To analyse the DGA of the nano-confined crystals, l_1, l_2 and l_3, as well as φ and d were determined from the optical micrographs. Raman and PL spectroscopies were carried out under ambient conditions using a commercial instrument (WITec alpha300 R) equipped with a 532-nm excitation laser. Polarization-resolved SHG characterization was conducted using a home-built setup (Supplementary Fig. 12) equipped with a 1,064-nm excitation laser (NPI Rainbow 1064 OEM). Cross-sectional samples for transmission electron microscopy were prepared with the lift-out technique using a focused ion beam (FIB; Helios G4 CX DualBeam). Aberration-corrected STEM imaging and EELS mapping were performed using a Nion Ultra-HERMES-100 microscope operated at 100 kV. HAADF-STEM images were acquired using a converge angle of 30 mrad and an annular detector with 92–210 mrad collection semi-angles. The software STEM_CELL[55] was used to perform the HAADF simulation of the Janus MoSSe monolayer according to the experimental settings of the microscope. The sample thickness was set to 10 nm. The thermal diffuse scattering was set to ten cycles. The source size broadening was considered in the simulation by including a Gaussian spread with a full width at half maximum (FWHM) of 0.8 Å.

Theoretical calculations

DFT calculations were performed using the Vienna Ab initio Simulation Package[56] and the projector augmented-wave method[57]. The exchange–correlation potential was described using the Perdew–Burke–Ernzerhof form of the generalized gradient approximation[58]. The vdW correction was considered using the DFT-D2 approach[59]. For the calculation of the binding energy of $NbSe_2$ monolayers, an energy cutoff of 400 eV was adopted for the plane-wave basis set, and the Brillouin zone was sampled using a $7 \times 7 \times 1$ **k**-point mesh. The energy and force convergence thresholds were set to 1.0×10^{-4} eV and 0.01 eV Å^{-1}, respectively. The binding energy was obtained according to $E_{\mathrm{binding}} = E_{\mathrm{total}} - E_{\mathrm{TMD}} - \sum E_{\mathrm{neighbour}}$, where E_{total} is the total energy of the adsorbing system, E_{TMD} is the energy of the isolated TMD monolayer and $E_{\mathrm{neighbour}}$ is the energy of the isolated neighbouring layer. As for the calculations of the energy of the substituted TMD monolayers (that is, $MoS_{2(1-x)}Se_{2x}$ and $MoS_{2x}Se_{2(1-x)}$) and the graphene/Janus MoSSe vdW gap, an energy cutoff of 300 eV was adopted, and the Brillouin zones were sampled using $2 \times 2 \times 1$ and $3 \times 3 \times 1$ **k**-point meshes, respectively. The energy convergence threshold was set to 1.0×10^{-6} eV, and the force convergence threshold was set to 0.01 eV Å^{-1}. The vacuum layer thickness was >10 Å for all DFT calculations. Phase-field simulations of the nano-confined growth shape and the precursor distribution were performed using a two-region model (Supplementary Fig. 14) that incorporates the edge-intercalation process. The detailed simulation method can be found in previous work[60].

Device fabrications and measurements

For the graphene/Janus MoSSe heterostructure devices, fabrication and measurement procedures are detailed in Supplementary Fig. 21. The intrinsically patterned $NbSe_2$ devices were fabricated by transferring the as-grown hBN/$NbSe_2$ heterostructures onto bottom metal electrodes using a polycarbonate-based stamping method[61]. The electrodes were prepared using photolithography (Karl Suss MA6/BA6) and electron-beam evaporation (AST Peva-600E; Cr/Au 5/20 nm), followed by lift-off in acetone. Device measurements were conducted using the Quantum Design Physical Property Measurement System, with the lowest accessible temperature of ~2 K. Resistance was measured in the two-terminal configuration using the resistivity option of the Physical Property Measurement System in alternating-current (AC) mode, with a typical excitation current of 100 nA.

Data availability

All data are available in the main text or the Supplementary Information. Source data are provided with this paper.

References

55. Grillo, V. & Rotunno, E. STEM_CELL: a software tool for electron microscopy: part I – simulations. *Ultramicroscopy* **125**, 97–111 (2013).
56. Kresse, G. & Furthmüller, J. Efficient iterative schemes for ab initio total-energy calculations using a plane-wave basis set. *Phys. Rev. B* **54**, 11169–11186 (1996).
57. Kresse, G. & Joubert, D. From ultrasoft pseudopotentials to the projector augmented-wave method. *Phys. Rev. B* **59**, 1758–1775 (1999).
58. Perdew, J. P., Burke, K. & Ernzerhof, M. Generalized gradient approximation made simple. *Phys. Rev. Lett.* **77**, 3865–3868 (1996).
59. Grimme, S. Semiempirical GGA-type density functional constructed with a long-range dispersion correction. *J. Comput. Chem.* **27**, 1787–1799 (2006).
60. He, W., Geng, D. & Xu, Z. Pattern evolution characterizes the mechanism and efficiency of CVD graphene growth. *Carbon* **141**, 316–322 (2019).
61. Purdie, D. G. et al. Cleaning interfaces in layered materials heterostructures. *Nat. Commun.* **9**, 5387 (2018).

Acknowledgements

We thank M. Ouyang for helpful discussions. This work was supported by the National Key R&D Program of China (2022YFA1204100), the National Natural Science Foundation of China (62488201) and the Chinese Academy of Sciences (XDB33030100 and XDB30010000). Y.Z. and F.D. acknowledge the startup grant and the High-Talent Grant (SIAT-SE3G0991010, 2023) from the Shenzhen Institute of Advanced Technology. R.G. and W.Z. acknowledge support from the National Natural Science Foundation of China (52373231) and the Beijing Outstanding Young Scientist Program (BJJWZYJH01201914430039). H.H. acknowledges support from the Chinese Academy of Sciences (XDB30000000). W.H. and Z.X. acknowledge support from the National Natural Science Foundation of China (52090032). This work benefited from support and resources from the Electron Microscopy Center at the University of Chinese Academy of Sciences.

Author contributions

H.-J.G. conceived the idea and designed the project. C.B., Q.Q., K.Z., H.W., K.W. and P.P. synthesized the samples. C.B. performed the Raman, PL and SHG characterizations and conducted the crystal thickness and DGA analyses. R.G., Z.W. and W.Z. performed the STEM/EELS characterizations. Y.Z., H.H. and F.D. performed the DFT calculations. W.H. and Z.X. performed the phase-field simulations. C.B and H.L. fabricated and measured the devices. C.B., H.L., H.G., F.D. and H.Y. analysed the growth mechanisms. C.B., H.L., W.Z., H.Y. and H.-J.G. wrote the paper with input from all authors.

Competing interests

The Institute of Physics, Chinese Academy of Sciences filed a Chinese patent application (202111202207.3), which lists C.B., H.Y. and H.-J.G. as the inventors. Other than that, the authors declare no competing interests.

Additional information

Supplementary information The online version contains supplementary material available at https://doi.org/10.1038/s41563-026-02495-9.

Correspondence and requests for materials should be addressed to Wu Zhou, Feng Ding, Haitao Yang or Hong-Jun Gao.

Peer review information *Nature Materials* thanks Vincent Tung and the other, anonymous reviewer(s) for their contribution to the peer review of this work.

Reprints and permissions information is available at www.nature.com/reprints.